Isotopes and the characterization of extrasolar planets

Zhang, Y.

4

Search for Helium airglow emission from the hot Jupiter τ Boo b

The helium absorption line at 10830 Å originating from the metastable triplet state 2^3S, has been suggested as an excellent probe for the extended atmospheres of hot Jupiters and their hydrodynamic escape processes, and has recently been detected in the transmission spectra of a handful of planets. The isotropic re-emission will lead to helium airglow that may be observable at other orbital phases. The goal of this paper is to investigate the detectability of He I emission at 10830 Å in the atmospheres of exoplanets using high-resolution spectroscopy, providing insights into the properties of the upper atmospheres of close-in gas giants. We estimate the expected strength of He I emission in hot Jupiters based on their transmission signal. We search for the He I 10830 Å emission feature in τ Boo b in three nights of high-resolution spectra taken by CARMENES at the 3.5m Calar Alto telescope. The spectra in each night were corrected for telluric absorption, sky emission lines and stellar features, and shifted to the planetary rest frame to search for the emission. The He I emission is not detected in τ Boo b, reaching a 5σ contrast limit of 4×10^{-4} for emission line widths of >20 km s^{-1}. This is roughly a factor ~8 above the expected level of emission (assuming a typical He I transit absorption of 1% for hot Jupiters). This suggests that targeting the He I emission with well-designed observations using upcoming instruments such as VLT/CRIRES+ and E-ELT/HIRES is possible.

🗎 **Zhang, Y.**, Snellen, I. A. G., Mollière, P., Alonso-Floriano, F. J., Webb, R. K., Brogi, M., & Wyttenbach, A. (2020) Search for He I airglow emission from the hot Jupiter τ Boo b. A&A, 641, A161.

4.1 Introduction

The atmospheres of close-in exoplanets are strongly affected by the high-energy irradiation from their host stars, making their upper atmospheres weakly bound and susceptible to hydrodynamic escape (Owen, 2019). For gas-giant planets, Lyman-α absorption in transit measurements has been the primary probe for their extended atmospheres, e.g., HD 209458b (Vidal-Madjar et al., 2003), GJ 436b (Ehrenreich et al., 2015, Kulow et al., 2014) and GJ 3470b (Bourrier et al., 2018). Such observations trace the exospheres with neutral hydrogen extending far beyond the Roche lobe radius, and cast light on the hydrodynamic escape and mass loss, which drives the evolution of the atmospheric and bulk composition of close-in exoplanets (Ehrenreich et al., 2015).

In addition to Lyα, helium at 10830 Å was also identified to be a powerful tracer of the extended atmospheres (Seager & Sasselov, 2000), which was recently reassessed by Oklopčić & Hirata (2018). This helium line has several advantages over Lyα because it suffers less from the interstellar absorption and can be observed from the ground with high-resolution spectrographs, opening a new window into the characterization of exospheres.

The theoretical work by Oklopčić & Hirata (2018) has resulted in a breakthrough in helium measurements. Excess absorption was first detected by the Hubble Space Telescope/Wide Field Camera 3 in WASP-107b (Spake et al., 2018) and independently confirmed by ground-based observations (Allart et al., 2019, Kirk et al., 2020) showing an absorption level of 5.54 ± 0.27%. In addition, another five planets have been reported with helium signals, namely, HAT-P-11b at a level of 1.08 ± 0.05% (Allart et al., 2018, Mansfield et al., 2018), HD 189733b at 0.88 ± 0.04% (Guilluy et al., 2020, Salz et al., 2018), WASP-69b at 3.59 ± 0.19% (Nortmann et al., 2018), HD 209458b at 0.91 ± 0.10% (Alonso-Floriano et al., 2019), and GJ 3470b at 1.5 ± 0.3% (Ninan et al., 2020, Palle et al., 2020). Upper limits in He I absorption were derived for Kelt-9b and GJ 436b at 0.33% and 0.41% (Nortmann et al., 2018), for WASP-12b at 59±143 ppm over a 70Å band (Kreidberg & Oklopčić, 2018), for GJ 1214b at 3.8%±4.3% (Crossfield et al., 2019a), for K2-100b with an equivalent width less than 5.7 mÅ (Gaidos et al., 2020), and AU Mic b with EW of 3.7 mÅ (Hirano et al., 2020).

The wide range of helium absorption levels seen in the transmission spectra of hot gas giants is likely due to the variety in the stellar radiation fields. The helium absorption line at 10830 Å originates from atoms in a metastable triplet state 2^3S, which is mainly populated via recombination of ionized helium. The ionization of He I requires photons with wavelengths smaller than 504 Å, i.e. X-ray and extreme-ultraviolet (EUV). Therefore, the helium absorption is expected to be enhanced for planets irradiated with higher X-ray and EUV flux (Nortmann et al., 2018). However, the level of EUV irradiation may not be the only determining factor. The mid-ultraviolet radiation near 2600 Å can de-populate the triplet state 2^3S via ionization. Therefore, the strength of the helium absorption has been proposed to depend on the ratio between EUV and mid-UV stellar fluxes, and K-type stars may provide the most favorable stellar environment (Oklopčić, 2019). Hitherto, the exoplanets with detected helium absorption generally support this trend with four out of six orbiting K-type stars. More detections will help to better understand the factors that affect the He I absorption level.

As helium atoms at the triplet state 2^3S absorb photons to reach 2^3P state, the opposite transition will happen concurrently, with 10830 Å photons re-emitted in random

directions. Based on the absorption level, we estimate the amount of emission expected from the planetary atmospheres. The study of He ɪ airglow emission allows for better understanding of the radiation fields and level populations under non-local thermodynamic equilibrium in the upper atmospheres. In addition, it provides a way of probing the extended atmospheres of non-transiting close-in gas giants, which have not been investigated before.

In this paper, we address the detectability of He ɪ emission in the atmospheres of close-in exoplanets. We first calculate the expected emission level (Section 4.2), then perform a case study on τ Boo b (Section 4.3) searching for helium airglow emission in high-resolution spectroscopic data from CARMENES (Calar Alto high-Resolution search for M dwarfs with Exoearths with Near-infrared and optical Echelle Spectrographs) in Section 4.4 and 4.5. We discuss our results and future prospects in Section 4.6.

4.2 Helium emission from extended atmospheres

The concept of probing He ɪ airglow emission is illustrated in Fig. 4.1. We consider the extended atmosphere as an optically thin cloud surrounding the exoplanet. The cloud absorbs a fraction of irradiation from the host star due to the transition at 10830 Å, resulting in the helium atoms at state 2^3S to be excited to the higher state 2^3P. The absorbed radiation is reemitted isotropically when the excited electrons jump back down to the metastable triplet state. Assuming the extended atmosphere has a low density and is optically thin, the reemitted photons can freely escape and be observed as an emission feature. We would like to point out that during transit the feature is seen in absorption because only a small fraction of the radiation is reemitted along the line-of-sight. Consequently, we can detect He ɪ absorption lines during transit, while emission lines from other viewing angles.

To estimate the strength of the He ɪ emission, the cloud is assumed to absorb a fraction of the incident stellar energy at 10830 Å, emitting it back isotropically. Assuming the upper energy level not being (de-)populated in another way, we can estimate (see Seager, 2010, Chap. 3)

$$4\pi R_c^2 F_c^S = F_*^S f_{\text{abs}} \left(\frac{R_*}{a} \right)^2 \pi R_c^2 \tag{4.1}$$

where R_c is the radius of the cloud that absorbs radiation at that wavelength, R_* is the stellar radius, a is the orbital distance of the planet, f_{abs} is the fraction of energy absorbed at 10830 Å, which is linked to the column density of helium atoms at state 2^3S in the cloud, F_c^S and F_*^S denote the 10830 Å flux at the surface of the planet and the star respectively. The corresponding fluxes that we observe at Earth are

$$\mathscr{F}_c = F_c^S \left(\frac{R_c}{D} \right)^2, \quad \mathscr{F}_* = F_*^S \left(\frac{R_*}{D} \right)^2 \tag{4.2}$$

where D is the distance of the system to Earth. Thus, the planet to star contrast at 10830 Å is

$$\frac{\mathscr{F}_c}{\mathscr{F}_*} = \frac{f_{\text{abs}} R_c^2}{4a^2} = \frac{R_*^2}{4a^2} T_\lambda = 10^{-4} \left(\frac{T_\lambda}{1\%} \right) \left(\frac{5}{a/R_*} \right)^2 \tag{4.3}$$

T_λ is the excess absorption at 10830 Å that can be measured by transmission spectroscopy, with $T_\lambda = f_{\text{abs}} R_c^2 / R_*^2$.

Uncertainties regarding this estimate are further discussed in Section 4.6.1. A more detailed derivation involving radiative transfer is presented in Appendix 4.A. Given Equation 4.3, we expect contrast levels of ~ 10^{-4}, which may be reached by combining multiple nights of observations.
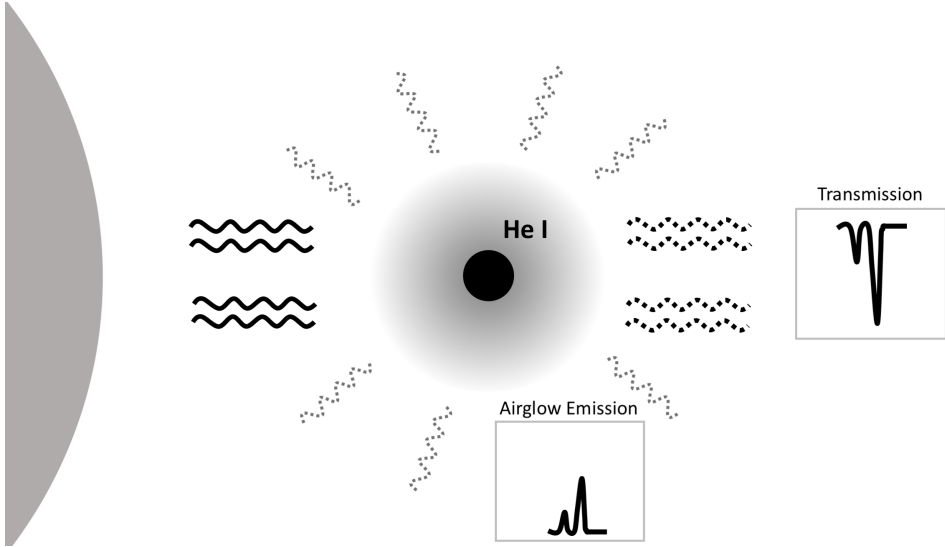

Figure 4.1: Illustration of He I emission from an exosphere of a close-in planet. The gray disk represents the extended atmosphere around such planet. He I absorption is observed during transit, while airglow emission can be probed at other orbital phases.

4.3 The τ Boo system

The hot Jupiter τ Bootis b is among the first exoplanets discovered (Butler et al., 1997), orbiting a bright F7V type main-sequence star (V=4.5 mag) at a distance of 15.6 pc from Earth. Although the planet is not transiting, its orbital inclination was determined to be 45° by tracking CO absorption in its thermal dayside spectrum (Brogi et al., 2012), confirmed by measurements of H_2O (Lockwood et al., 2014). The properties of the τ Boo system are summarized in Table 4.1. Unfortunately, because the planet is not transiting, there is no direct measure of its radius (meaning that its surface gravity is unknown), and the He I 10830 Å line cannot be probed in transmission.

The system has been an interesting target for investigating star-planet interactions because of its strong stellar activity. The star has a high S-index of 0.202 (Wright et al., 2004), indicating strong emission cores in the Ca II H&K lines. It exhibits an X-ray luminosity of 9×10^{28} erg s^{-1} (Huensch et al., 1998), and a reconstructed EUV luminosity of 2.5×10^{29} erg s^{-1} (Sanz-Forcada et al., 2011), which are among the highest values found in the planet-hosting stars. The intense X-ray and EUV radiation can deposit substantial energy in the planetary atmosphere, facilitating the expansion and evaporation of gas. Although τ Boo is not a K-type star (which is possibly the most favorable spectral type for probing the helium line), however, due to the high level of stellar X-ray and EUV emission, τ Boo b

could well have an extended atmosphere with a large population of helium at the triplet state, and forms a promising target to search for the He I emission at 10830 Å.

Table 4.1: Properties of the star τ Boo (upper part) and τ Boo b (lower part).

Parameter	Symbol	Value
Distance (pc) [a]	d	15.66 ± 0.08
Effective temperature (K) [b]	T_{eff}	6399 ± 45
Luminosity ($L_\odot$) [b]	L_*	3.06 ± 0.16
Mass ($M_\odot$) [b]	M_*	1.38 ± 0.05
Radius ($R_\odot$) [b]	R_*	1.42 ± 0.08
Surface gravity (cgs) [c]	$\log g$	$4.27^{+0.04}_{-0.02}$
Systemic velocity (km s^{-1}) [d]	γ	-16.4 ± 0.1
Rotation velocity (km s^{-1}) [b]	$v \sin(i)$	14.27 ± 0.06
Semi-amplitude (m s^{-1}) [e]	K_*	468.42 ± 2.9
Metallicity (dex) [b]	[M/H]	0.26 ± 0.03
Age (Gyr) [b]		0.9 ± 0.5
Orbital period (days) [e]	P	$3.312454 \pm 3.3 \cdot 10^{-6}$
Semi-major axis (AU) [b]	a	0.049 ± 0.003
Orbital inclination (deg) [d]	i	44.5 ± 1.5
Eccentricity [b]	e	0.011 ± 0.006
Mass (M_J) [b]	M_p	6.13 ± 0.17
Phase zero-point (HJD) [e]	T_0	56401.8797 ± 0.0036
Semi-amplitude (km s^{-1}) [d]	K_P	110.0 ± 3.2

[a] Gaia Collaboration et al. (2018);
[b] Borsa et al. (2015);
[c] Takeda et al. (2007);
[d] Brogi et al. (2012);
[e] Justesen & Albrecht (2019)

4.4 Observations and Data analysis

We observed and analyzed the τ Boo system for five nights with the CARMENES spectrograph mounted on the 3.5m Calar-Alto Telescope (Quirrenbach et al., 2016), on 26 March 2018, 11 May 2018, 12 March 2019, 15 March 2019 and 11 April 2019. CARMENES has two channels, VIS and NIR, covering the optical wavelength range (520-960 nm) and the near-infrared wavelength range (960-1710 nm) respectively. The resolving power is 94,600 in the VIS channel and 80,400 in the NIR channel. Each channel is fed with two fibers: fiber A targeting the star and fiber B obtaining a sky spectrum simultaneously. The He I line at 10830 Å falls on echelle order 56 (10801-11001 Å) in the NIR channel, on which we focused our analysis.

The details of the observations are shown in Table 4.2 and Fig. 4.2. The observations probed thermal emission from τ Boo b, covering a wide range in planet orbital phases each night (see Fig. 4.2). The exposure times were adjusted according to the weather conditions, maintaining a S/N≥100. The observations in the first two nights were taken with exposure

times of 40 s with a seeing of 2″ and 1.4″ respectively, delivering lower S/N per spectrum than during the other nights with longer exposures and better weather conditions. The drop-off in S/N during the end of night 2 was due to the increasingly high airmass. The relative humidity during night 1, 2 and 5 continuously exceeded 85%, in contrast to the lower value (~45%) during night 4. This agrees well with the behavior of S/N in these nights. For night 3, although the relative humidity was not as high as the first two nights, it underwent strong variation overnight, possibly accounting for the drastic change in S/N.

The standard data reduction, such as bias removal, flat fielding, cosmic ray corrections, and wavelength calibration, was performed with the CARMENES pipeline CARACAL v2.10 (Caballero et al., 2016). The output of the pipeline was provided in the observer's frame with a vacuum wavelength solution. We converted the vacuum wavelength solution into air wavelengths and used it throughout our analysis.
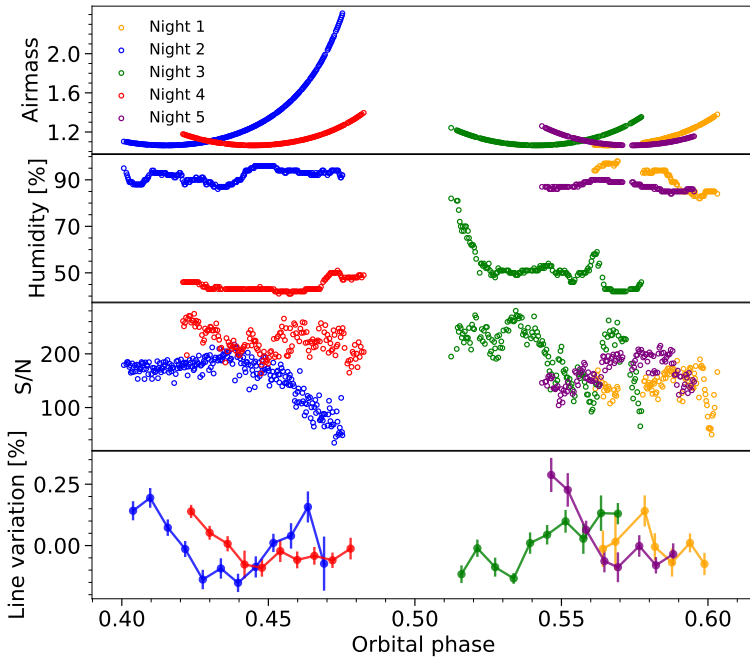

Figure 4.2: Variation in airmass (upper panel), relative humidity (mid panel), S/N (lower panel) and variation around the mean of the stellar He I line (bottom panel) during observations in the different nights. The S/N of each spectrum is defined as the average signal-to-noise ratio of the continuum near the He I 10830 Å line.

4.4.1 Data analysis

First, we manually corrected for additional hot pixels and cosmic rays present in the pipeline-reduced spectra by substituting those values with the linear interpolation of adjacent pixels or adjacent time series. Subsequently, each spectrum was normalized to unity using the continuum both at the blue and red side of the helium line over the
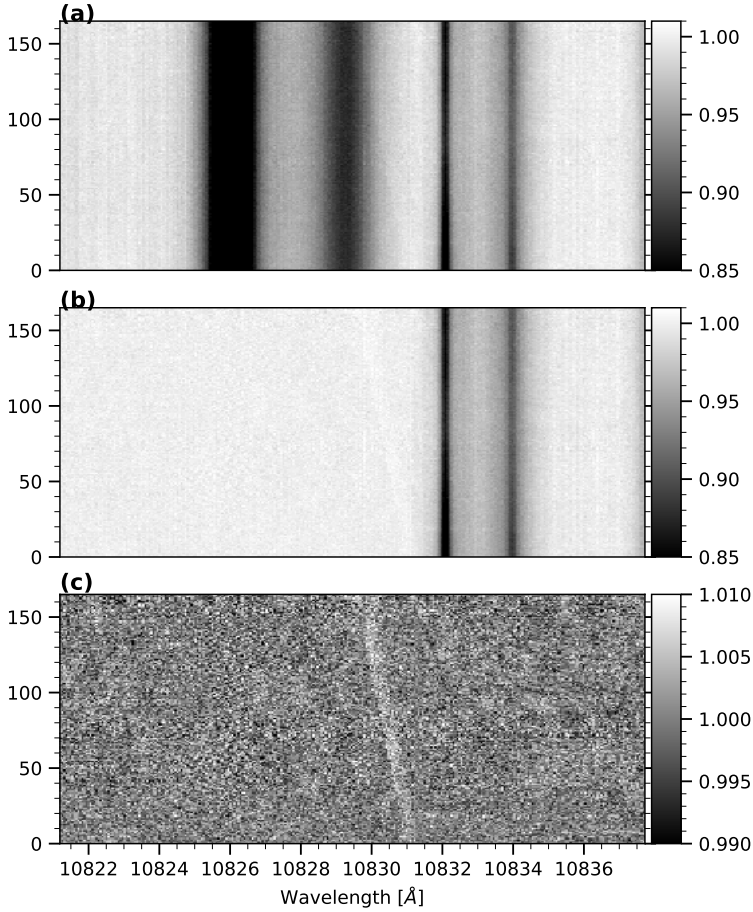
Figure 4.3: Illustration of our data reduction steps applied to the spectral series taken on Night 4. Each row in the matrix represents one spectrum, with the y-axis corresponding to time. As detailed in Section 4.4.1, the steps include: (a) normalization of the continuum; (b) correction for stellar lines in each spectrum using an empirical model; (c) removal of telluric contamination by correcting the temporal variation of the flux in telluric lines using a column-by-column linear regression. The trail of an artificially injected planetary helium line (with a magnitude of 0.3% and a width of 11 km s^{-1}) can be seen as a slanted white band near 10830 Å, shifting in time due to the change in the radial component of the orbital velocity of the planet.

Table 4.2: Observations Summary

Night	Date	Proposal No.	Program PI	No. of spectra	Exposure time (s)	On-target time (h)	S/N
1	2018-03-26	F18-3.5-012	J.A.Caballero &	110	40	1.2	140
2	2018-05-11	F18-3.5-012	F.J.Alonso-Floriano	261	40	2.9	160
3	2019-03-12	F19-3.5-051	M.Brogi	161	66	3.1	200
4	2019-03-15	F19-3.5-051	M.Brogi	165	65	3.0	220
5	2019-04-11	F19-3.5-051	M.Brogi	133	66	2.4	170

ranges 10804.0-10805.2 Å, 10818.5-10819.0 Å and 10839.0-10840.3 Å. After normalization, the spectral series of each night were handled as a two-dimensional matrix as shown in Fig. 4.3(a). Each row in the matrix represents one spectrum, with the frame number on the y-axis, corresponding to orbital phase or time.

Before correcting for the telluric lines, we first removed the stellar Si line and He I triplet at 10827.1 Å and 10829.09, 10830.25 and 10830.34 Å. In order to achieve this, we built an empirical stellar model for each night by combining all spectra with S/N>100 in the stellar rest frame, where we set all values outside of the two stellar features to unity. This model was then shifted to the observer's rest frame, scaled and removed from each spectrum. Subsequently, the spectra were free of stellar lines in the wavelength region near the planetary helium line (see Fig. 4.3(b)).

The residual matrix in Fig. 4.3(b) shows the telluric lines near the planetary helium signal that required removal, including the H_2O absorption features at 10832.1 Å and 10834.0 Å, and the OH emission lines at 10824.7 Å, 10829.8 Å and 10831.3 Å. The strengths of telluric lines vary overnight, which mainly results from the change in airmass and/or water column. To correct for telluric absorption lines, we measured the temporal variation of the flux at the centers of several deep H_2O absorption features and combined them to serve as a representation for the atmospheric change overnight. Such temporal variation was then removed using a column-by-column linear regression while avoiding the columns that contain the assumed planetary He I emission. We removed the sky emission lines in a similar way, using their mean-variation overnight. After telluric correction, each column of the matrix was subsequently normalized as follows. The spectra were combined via weighted average, with the weights defined as the squared S/N of each exposure, to build a master spectrum. Each individual spectrum was subsequently divided by this master spectrum to obtain the residual spectral series as shown in Fig. 4.3(c).

We note that during the telluric removal and final normalisation, we masked the region in each spectrum where the planetary He line is expected to appear, so that we could avoid self-subtraction of the signal, if present. This is particularly important if the planetary He I line is broad. In the case that the line width is larger than the change of the planetary radial velocity overnight, the planetary signal would be (partially) subtracted out, making it less likely to be detected.

4.4.2 Extra noise in residual spectra

After correcting for the stellar and telluric effects, we shifted the residual spectral series of all five nights into the stellar rest frame by correcting for the systemic velocity, barycentric velocity, and stellar reflex motion of τ Boo, as shown in Fig. 4.4. The spectra were binned to 0.006 in phase (y-axis) for a better identification of the noise structure. We noticed that the observations in nights 2 and 3 suffer from broad noise structures, which may originate from the variability of stellar lines or the residuals of telluric corrections.

As we noted in section 4.3, the star τ Boo shows a high level of chromospheric activity. The stellar He I line as a chromospheric diagnostic may undergo temporal variation due to flaring. The strength of the stellar He I line can also show periodic modulation by rotation if the line is not homogeneous on the stellar disk (Andretta et al., 2017). Moreover, the fast spin of τ Boo may result in residual noise features shifting in wavelength up to its rotation velocity (~15 km s^{-1}). To quantify the effect of stellar variability, we measured the strength
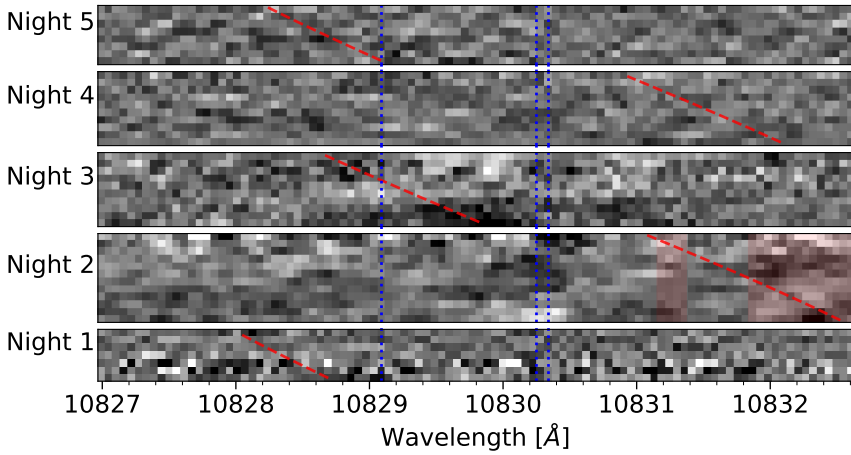
Figure 4.4: Residual spectral series from night 1 to 5. The y-axis represents the time or orbital phase. The residuals are binned to 0.006 in phase for clarity. The slanted dashed lines in red trace the expected planetary helium line. The dotted lines in blue denote the positions of the stellar He I triplet. The shaded region in night 2 contains the telluric H_2O absorption and OH emission line, overlapping with the expected planetary helium line.

of the stellar He I line at 10830 Å during each night by fitting a Gaussian profile to the data and measuring the amplitude of the best-fit Gaussian profile. We define the line variation as the relative depth with respect to the average stellar spectrum of each night, and then bin the results to 0.006 in phase (see Fig. 4.2 bottom panel). During a single night, the variation is generally ≤0.25%, which is within the noise level of the data, therefore should not significantly affect our analysis. However, it is possible that the variation can build up as we combine different frames during the night, leading to systematic noise in the combined residual spectrum. For example, the variability of He I line may be responsible for the variation in the residual flux at 10830.3 Å in night 2 (see Fig. 4.4). We also compared the average line profile of different nights (Fig. 4.5). On a night-to-night basis, we note that the helium line profile in night 2 is distinct from other nights, perhaps due to the influence of the nearby strong telluric line or the higher level of stellar activity.

In addition, we note that the spectral S/N in the middle of night 3 abruptly dropped by a factor of two as shown in Fig. 4.2, probably due to the changing weather condition. This may lead to the inconsistency of the data in the region from 10829.4 to 10830.2 Å. Unfortunately, the trail of the planetary signal in night 3 resides exactly in this problematic wavelength range, overwhelmed by artifacts (see Fig 4.4). As for the night 2 observations, telluric lines show a high level of strength and variability due to the high relative humidity and the variation of the precipitable water vapor, which could not completely be removed. The residuals of the deep telluric H_2O line at 10832.1 Å and OH sky emission at 10831.3 Å coincide with the trail of the planetary signal (see Fig 4.4), making it difficult to preserve it while removing the telluric contamination. In such condition, adding the night 2 data does not enhance the S/N because more noise was introduced along with the diminished signal. Consequently, we excluded the observations of night 2 and 3 from further analysis.

Based on the ephemeris listed in Table 4.1, we shifted the residual spectra to the plan-
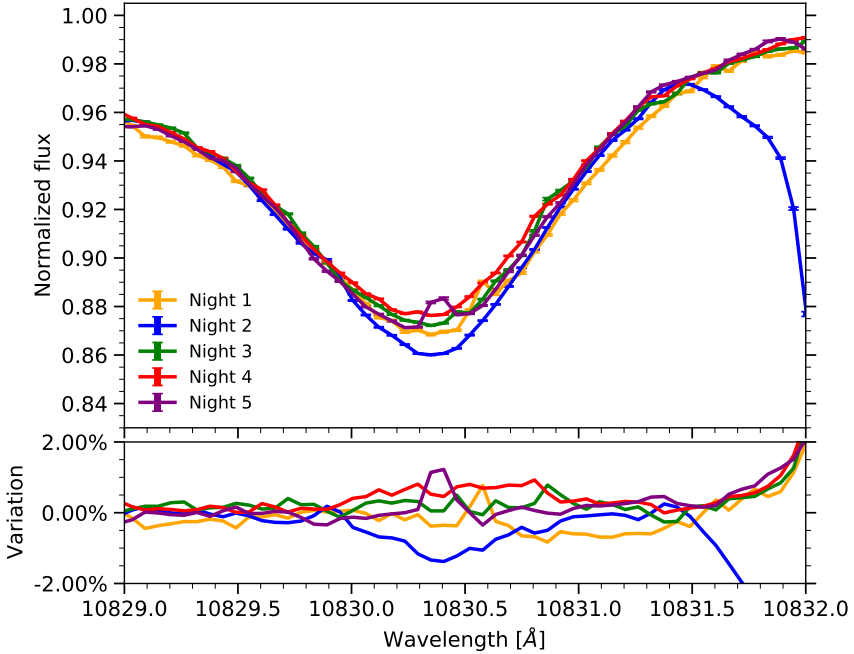
Figure 4.5: Upper panel: the average profile of the stellar helium line in each night. Lower panel: the difference of each profile with respect to the mean. The deep absorption line at 10832.2 Å in night 2 (blue curve) is a telluric H_2O line. The small peaks on top of the helium line in night 1 and 5 are caused by sky OH emission.

etary rest frame. The residual spectral series from different nights were then combined with each residual spectrum weighted by its variance over the radial velocity ranges from -150 to -50 km s^{-1}and from 50 to 150 km s^{-1}.

4.5 Result

Fig. 4.6 shows the time-averaged spectrum around the helium line in the planet rest-frame, with the amplitude scaled to make the standard deviation equal to unity around the targeted He I 10830 Å line. We find no statistically significant signal from the planetary He I 10830 Å line within the three nights of observations.

4.5.1 Detection limits

As we have no information on the profile of the potential He I line originating from τ Boo b, we assumed a box profile centered at 10830.3 Å, which has a clear definition of the line width compared to a Gaussian profile. We performed signal injections considering various widths (W) of the planetary emission, ranging from 3.7 km s^{-1}(equal to the instrument resolution) to 37 km s^{-1}(which is limited by the self-subtraction of broad signals). The combined residuals of both the observations and injections are shown in Fig. 4.6 for three different line widths as examples. We regarded the original residuals (without signal
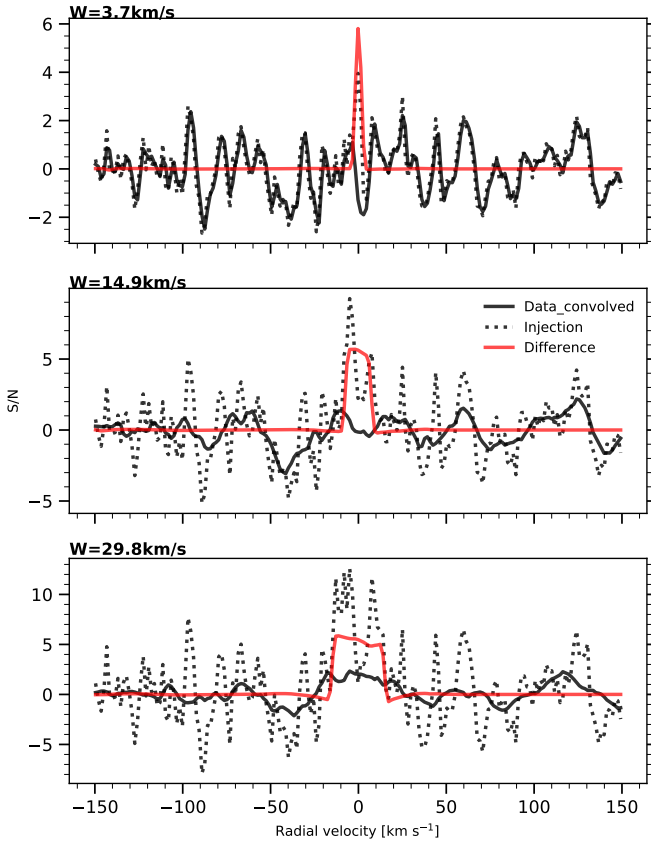
Figure 4.6: Combined (3 nights) residual spectra in the planetary rest frame centered at the 10830 Å He I line. In the three panels, the solid black line indicates the residual spectra, boxcar-smoothed by 3.7 km s^{-1}(top), 14.9 km s^{-1}(middle), and 29.8 km s^{-1}(bottom). The dotted curves show an artificially injected signal at a S/N of 5, with the solid red curve the difference between the injected and original data. The values are scaled by the standard deviation of the observed residuals so that the y-axis represents the S/N.

injection) as the noise, and convolved it with the corresponding signal profile to take the width of the signal into account. The noise level is defined as the standard deviation (from -150 to +150 km s^{-1}) of the convolved residuals. These were then scaled by this noise level, so that the y-axis represents the signal-to-noise ratio (S/N). The strength of the signal in each injection case was determined by measuring the amplitude of the recovered signal, which is the difference between the injected and the original residuals, as shown by the red curves in Fig. 4.6. The 5σ detection limits were thus determined as the minimum line emission leading to a recovered S/N of 5 in our injection tests. The detection limit as a function of the line width is shown in Fig. 4.7. We note that the S/N is determined at the peak of the emission signal (namely the amplitude of the box profile). Therefore, detecting a broader signal requires a lower level of the peak contrast, as shown in the black line in Fig. 4.7. However, this does not mean that the detectability increases when it comes to

broad signals. As the flux is distributed into wider velocity space due to broadening mechanisms, it actually requires larger amount of integrated flux (namely higher Equivalent Width) to detect broader signals. The corresponding Equivalent Width limit required for 5σ detection is plotted in the red curve in Fig. 4.7.

The width of the signal is affecting the S/N of a potential detection in the following ways. First, the level of white noise decreases with the square root of the line width. Although the residual noise in our case is not fully uncorrelated due to imperfect stellar and telluric corrections, the S/N can still be enhanced, if not as much as by a factor of $\sqrt{W}$. Secondly, for a larger W a wider part of the planet emission line trail is masked out, changing the residual noise pattern of the data, as shown in Fig. 4.6, where the observed residuals (solid black curves) for different widths are not identical. Furthermore, the detection of broad planetary signals is hindered by the self-subtraction problem as discussed in section 4.4.1. Hence, the detectability drops significantly for widths larger than 25 km s^{-1}, which is comparable to the radial velocity change of the planet during a night. Overall, the detection limit drops significantly towards larger W, but reaches a plateau at $W > 20$ km s^{-1}, for which we reach a 5σ limit of 4×10^{-4}.
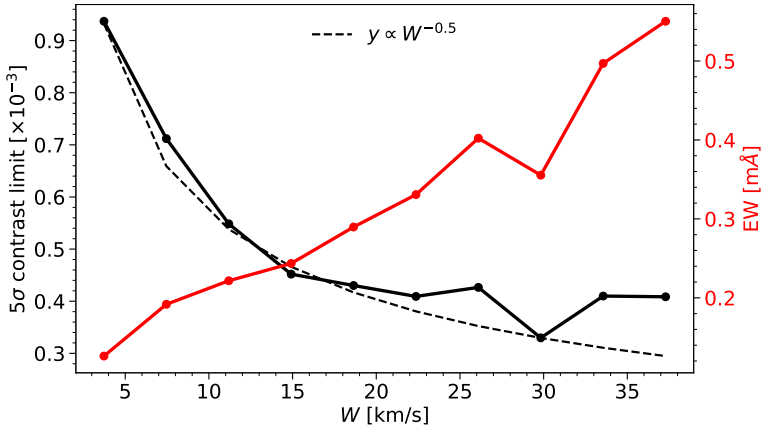

Figure 4.7: The 5σ detection limit of the He $\textsc{i}$ airglow emission as a function of the line width of the potential signal using 3 nights of observations of τ Boo b (solid black line), and corresponding equivalent widths of the detection limit (solid red curve). The dashed line represents a scaled relation of $W^{-1/2}$, expected for pure Gaussian white noise.

4.5.2 Validation of signal recovery

Prior knowledge of the planetary orbit was used to mask the trail in the spectral series to avoid self-subtraction of the potential signal (see section 4.4.1). In order to assess the influence of this procedure on the final result, we repeated the whole analysis adopting a grid of planetary orbits with different semi-amplitude K_P and phase offset $\Delta\phi$ when applying the mask. In Fig. 4.8, we mapped the S/N of the residuals at 10830.3 Å in the planetary rest frame for each hypothetical orbit in the grid. As a comparison, we produced a similar map when injecting an artificial planetary signal with a strength of 3.3×10^{-4} and

a width of 30 km s^{-1}, which is recovered at K_P = 110 km s^{-1}and $\Delta\phi$ = 0 in Fig. 4.8, also without prior knowledge of the planetary orbit.
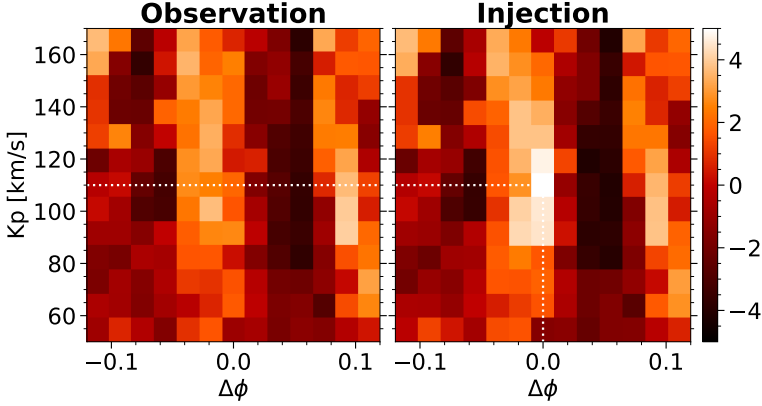

Figure 4.8: The S/N map for a grid of planetary orbits with different semi-amplitude K_P and phase offset $\Delta\phi$. There is no salient signal in the observations (left panel). An injected signal at K_P = 110 km s^{-1}and $\Delta\phi$ = 0 is clearly recovered (right panel).

4.6 Discussion

4.6.1 Detectability of He emission

Using three nights of observations (~6.5 hours of integration) on τ Boo b using CARMENES, we reached a contrast limit of 4×10^{-4} for a planetary He I emission with a boxcar profile with a width > 20 km s^{-1}. However, following Equation 4.3, the estimated amplitude of the He I emission is typically $\leq 10^{-4}$. At this stage, no detection is expected with these observations.

We note that we made several assumptions for simplicity. First, we assume the atmosphere extends significantly beyond the planet radius and the He I cloud is considered to be optically thin. The stellar radiation is absorbed uniformly in the cloud and reemitted isotropically. In addition, Equation 4.3 assumes that the energy is conserved at the particular wavelength 10830 Å, meaning that we only take into account the transition between the helium 2^{3}S and 2^{3}P states.

In practice, the flux ratio can deviate from this simplified model in the following ways. (a) The flux emission of the cloud can be higher than our estimation if the extent of the exosphere is even larger than the stellar disk, in which case the measured f_{abs} in the transmission spectrum is lower than the actual absorption level of the entire cloud. (b) Analysis on the line ratio of He I triplet detected in transmission observations suggests that the planetary signal could also originate from an optically thick part of the atmosphere, especially for Jupiter-mass planets such as HD 189733b and HD 209458b, where the He I absorption feature traces compact atmospheres with an extent of only a fraction of planetary radii (Lampón et al., 2020, Salz et al., 2018). If the cloud is not optically thin or the He I atmosphere is not significantly larger with respect to the planet, the reradiation is not

isotropically emitted from the cloud in 4π but with preferential directions, as an analogy to scattered light. In this case, the emission flux at the full phase (i.e. when the illuminated hemisphere is totally in view) is enhanced as compared to the value in Equation 4.3, yet it also needs to be scaled with the phase function Φ_α at different orbital phases (where we observe different portions of the illuminated hemisphere). (c) If the He I cloud is not optically thin, the planetary thermal emission passing through the cloud can be absorbed along the line of sight, which cancels out a portion of the airglow emission. To evaluate this effect, we compare the absorbed thermal emission to the airglow emission flux as follows. Assuming the planet emits as a blackbody with an equilibrium temperature of T_p, we can calculate the planetary thermal emission flux in contrast to the stellar flux at 10830 Å. Taking τ Boo system as an example, the flux contrast is $\mathscr{F}_{th}/\mathscr{F}_* \sim 10^{-5} \sim 0.25\mathscr{F}_c/\mathscr{F}_*$. To the optically thick limit, where all thermal emission is absorbed by the He I cloud, it counterbalances ~25% of the airglow emission. Consequently, even in the extreme optically thick case, the helium is expected to be seen in emission. (d) The emission level of He I 10830 Å is determined by the population of helium in the 2^3P state as well as the rates of the stimulated and spontaneous decay of 2^3P state. Studying this requires detailed accounts and comparisons of other de-populating processes including photoionization from 2^3P state, electron/H-atom collisions, and radiative excitation to 2^3D state (D3 line). Previous models of helium atmospheres, such as Lampón et al. (2020), Oklopčić & Hirata (2018), neglect transitions related to 2^3P state because the metastable 2^3S state population is not significantly affected by these processes as an atom in 2^3P state just decays back to 2^3S state (Oklopčić & Hirata, 2018). This indicates that the 2^3P to 2^3S decay is the major way of de-populating the 2^3P state. Therefore, we can argue for the connection between the level of absorption and airglow emission at 10830 Å.

In addition to the amplitude of the He I emission, the velocity profile is rather uncertain. Current detections suggest that the He I excess absorption spans a wide range of line widths. For instance, Saturn or Neptune mass planets such as WASP-69b and HAT-P-11b (Allart et al., 2018, Nortmann et al., 2018) are reported to have broad absorption feature (up to ~30 km s^{-1}), while Jupiter-mass planets such as HD 209485b (Alonso-Floriano et al., 2019) show a more narrow signature of ~10 km s^{-1}, implying a lower rate of atmospheric escape and mass loss. The line profile depends on the physical and hydrodynamic properties such as the kinematic temperature of the exosphere and the atmospheric escape, which are not well understood (Salz et al., 2016). Considering the diverse nature of planetary atmospheres, it is therefore recommended to explore a variety of line widths and line positions in data analysis.

4.6.2 Future prospects

Observation design

Based on our data analysis, we find several aspects that should be taken into account when designing future observations to search for He I airglow emission. Firstly, the observations should avoid blending the planetary helium signal with strong telluric absorption lines (such as during our night 2 observations). In such situation, a large portion of the emission signal is removed along with the telluric correction. Even if the signal is preserved with other methods, strong telluric features cannot be corrected perfectly, introducing artifacts around the helium signal. Furthermore, the S/N of observations at the core of strong

telluric absorption lines is significantly lower than in the continuum. Hence, the potential signal falling in such region is more difficult to detect. Therefore, taking into account the relative position between the planetary and telluric lines, and selecting the proper time for observations according to the barycentric Earth radial velocity (BERV) and the planetary radial velocity are desirable.

The stellar activity is yet another factor to consider in data analysis because the stellar He I line as a chromospheric diagnostic may undergo temporal variation during observations. For an active star like τ Boo , this is likely to happen and introduce extra noise. Cauley et al. (2018), Salz et al. (2018) and Guilluy et al. (2020) evaluated the impact of stellar activity on probing the planetary helium atmosphere in transmission. However, unlike transit observations, additional noise related to stellar activity should not significantly affect measurements of emission signals from a planet, because there is always a radial velocity offset between the star and planet when probing emission. Only when the radial velocity difference is small (that is, during transit and secondary eclipse), can stellar activity contribute to noise at the planetary rest frame and result in pseudo-signals. In terms of detecting airglow emission, the likely consequence of the variability of stellar He I line is to introduce systematic noise structure nearby the planetary signal in the temporal-combined residual spectrum, instead of affecting the level of planetary signal. Consequently, for highly active stars, there needs to be sufficient difference between the planet and stellar radial velocity, which depends on the orbital phase, during observations.

In terms of target selection, we performed the case study on τ Boo because the star is significantly brighter than other known hot-Jupiter systems, enabling high S/N observations. In addition, its high level of stellar activity likely results in an extended planetary atmosphere with the He I 2^3S populated. As shown in Fig 4.9, accounting for both the stellar brightness and the airglow emission signal estimated using Equation 4.3, τ Boo b falls closest to our detection limit (denoted by the dashed line) among other potential targets. In the emission signal calculation, as we have no measurements of the He I absorption by the non-transiting τ Boo b, we assume an absorption level of 1%, which, however, brings about some uncertainty. τ Boo as an F-type star may also have high levels of mid-UV radiation that can de-populate the helium triplet states, leading to a weaker signal. It remains unclear to what extent these various factors contribute to the He I signal as a whole. In addition, the planet mass is significantly higher than that of most hot Jupiters, increasing the surface gravity, possibly making atmospheric escape more difficult (Salz et al., 2016). A more secure choice is to investigate those targets with He I absorption already measured via transmission spectroscopy (denoted with red dots in Fig 4.9), so that we have an expectation of the emission amplitude beforehand. Another benefit of targeting a transit planet is that we could obtain the stellar spectrum without any contribution from the planet during secondary eclipse. Using that as a reference spectrum, we can avoid self-subtracting the planetary signal in analysis, which is particularly important for broad signatures. Furthermore, as discussed in Section 4.6.1, the airglow emission signal is partially counterbalanced by absorption of planet thermal emission through the He I cloud when it is compact. Consequently, planets with puffy and optically thin He I clouds are better targets for this purpose.
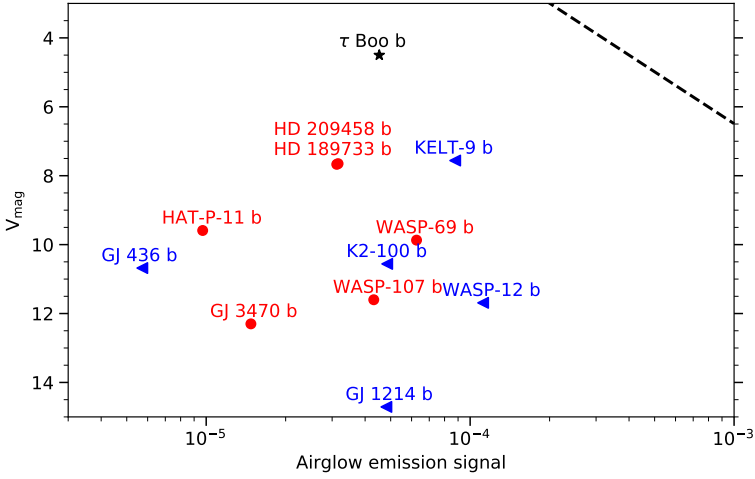
Figure 4.9: The V magnitude of host stars plotted against the airglow emission signal estimated using Equation 4.3 for exoplanets with He I absorption detections (in red dots) or upper limits (in blue triangles). The black star represents the estimated signal of τ Boo b assuming a typical absorption level of 1%. The black dashed line shows the detection limit of our analysis.

Search with VLT/CRIRES+ and E-ELT/HIRES

CRIRES+ is an upgrade of the cryogenic high-resolution infrared echelle spectrograph (CRIRES) located at the focus of UT1 of the Very Large Telescope (VLT), providing a spectral resolving power of 100,000 (Follert et al., 2014). If we simply scale the expected S/N for observations with CRIRES+ by the larger telescope diameter of the 8.2m VLT compared to the 3.5m Calar Alto Telescope, also considering that the throughput of CRIRES+ may be a factor of 1.5 lower than that of CARMENES, while the observing condition at VLT site is generally better, we expect in the same observing time to go a factor ~2 deeper. Accordingly, we expect to reach a detection limit of 2×10^{-4} for a broad He I emission given the same amount of integration (~6.5 hours). Taking τ Boo b as an example, following Equation 4.3, we estimate the amplitude of the emission to be ~ 5×10^{-5} assuming a typical "transit" absorption level of 1%. This means that a 3σ detection of He I airglow emission could be obtained in ~5 nights of observations. Although probing He I emission is demanding using the current generation of telescopes, it is promising with the High Resolution Spectrograph (HIRES) at ESO's forthcoming Extremely Large Telescope (E-ELT) (Marconi et al., 2016). Thanks to the significantly larger diameter of the 39m E-ELT, the 5σ detection of He I airglow emission could be achieved with ~3 hours of integration. Of course there is a large uncertainty in the expected level of emission, which can be at least partly mitigated by choosing a transiting planet.

4.7 Conclusions

This paper explores the possibility of probing He I emission at 10830 Å in the extended atmospheres of hot Jupiters, the amplitude of which is estimated based on the He I ab-

sorption level as observed during transit. We search for this emission from τ Boo b using CARMENES spectra. We correct for the telluric and stellar features nearby the expected He I signal and combine multiple nights of observations. Given our estimation of the contrast of $\leq 10^{-4}$, the 6.5-hour data combined is not sufficient to put meaningful constrains on the He I emission from the planet. The detection limit that we derive from our analysis is 4×10^{-4} for a broad emission signal with a width of >20 km s^{-1}. While we do not reach the required contrast with the current CARMENES data, the He I airglow emission from hot-Jupiters is still promising to probe with future instruments.

4.A Derivation of helium emission strength with radiative transfer

During transit, the stellar flux $\mathscr{F}_*$ decreases by $\Delta\mathscr{F}_*$ due to the absorption by helium atoms at 2^3S state. The absorption depth T_λ measured by transmission spectroscopy is

$$T_\lambda = \frac{\Delta\mathscr{F}_*}{\mathscr{F}_*} = \frac{R_c^2}{R_*^2} f_{\mathrm{abs}} = \frac{R_c^2}{R_*^2}(1 - e^{-\tau_c}), \tag{4.4}$$

where τ_c is the optical depth of the He I cloud around the planet, and the structure of the cloud is neglected.

4.A.1 Optically thick

For optically thick clouds, namely, $\tau_c \gg 1$, Equation 4.4 becomes

$$R_c = R_* \sqrt{T_\lambda} \,. \tag{4.5}$$

The emission flux from the cloud can be approximated as isotropic scattering with an albedo of 1, resulting in a factor of 2/3 of the received flux (Seager, 2010, Chap. 3):

$$F_c^S = \frac{2}{3}F_*^S\left(\frac{R_*}{a}\right)^2. \tag{4.6}$$

Substituting Equation 4.2 and 4.5 into Equation 4.6, we get

$$\frac{\mathscr{F}_c}{\mathscr{F}_*} = \frac{2}{3}\frac{\Delta\mathscr{F}_*}{\mathscr{F}_*}\left(\frac{R_*}{a}\right)^2 = \frac{2}{3}T_\lambda\left(\frac{R_*}{a}\right)^2. \tag{4.7}$$

4.A.2 Optically thin

For optically thin cases, we consider the simplified 1D plane-parallel equation of radiative transfer

$$\frac{dI}{d\tau} = I(\tau) - S(\tau), \tag{4.8}$$

where I_ν is the spectral radiance, S is the source function, and τ is the extinction optical depth which increases towards interior of the cloud (i.e. the optical depth at the interior is τ_c and that at the surface is 0).

The source function is approximated as

$$S(\tau) = J_*(\tau) = \frac{1}{4\pi} \int I_*(\tau) d\Omega = \frac{1}{4\pi} \left(\frac{R_*}{a}\right)^2 F_*^S e^{-\tau}. \tag{4.9}$$

Hence, the solution for the equation of radiative transfer can be composed as

$$I(\tau) = c e^{\tau} + \frac{1}{8\pi} \left(\frac{R_*}{a}\right)^2 F_*^S e^{-\tau}. \tag{4.10}$$

Using the boundary condition $I(\tau_c) = 0$, the integral constant c is determined, making the solution simplified as

$$I(\tau) = \frac{1}{8\pi} \left(\frac{R_*}{a}\right)^2 F_*^S (e^{-\tau} - e^{\tau - 2\tau_c}). \tag{4.11}$$

Then the emergent radiance from the cloud I_c is

$$I_c = I(0) = \frac{1}{8\pi} \left(\frac{R_*}{a}\right)^2 F_*^S (1 - e^{-2\tau_c}). \tag{4.12}$$

The observed flux of the cloud is

$$\mathscr{F}_c = \int I_c \left(n_c \cdot n_{\text{detector}}\right) d\Omega = \frac{1}{8\pi} \left(\frac{R_*}{a}\right)^2 F_*^S (1 - e^{-2\tau_c}) \frac{\pi R_c^2}{D^2}, \tag{4.13}$$

where n_c and n_{detector} represent the unit vectors along the intensity of the cloud and the normal direction of the detector surface respectively. Since the targets are far away, we can safely assume $n_c \cdot n_{\text{detector}} = 1$ in Equation 4.13.
Substituting $\mathscr{F}_* = F_*^S R_*^2 / D^2$ and Equation 4.4 into Equation 4.13, we have

$$\mathscr{F}_c = \frac{1}{8} \Delta F_* \left(\frac{R_*}{a}\right)^2 \frac{1 - e^{-2\tau_c}}{1 - e^{-\tau_c}}. \tag{4.14}$$

At the optically thin limit ($\tau_c \ll 1$), Equation 4.14 reduces to

$$\frac{\mathscr{F}_c}{\mathscr{F}_*} = \frac{1}{4} \frac{\Delta \mathscr{F}_*}{\mathscr{F}_*} \left(\frac{R_*}{a}\right)^2 = \frac{1}{4} T_\lambda \left(\frac{R_*}{a}\right)^2, \tag{4.15}$$

which agrees with Equation 4.3.